

InstantSfM: Fully Sparse and Parallel Structure-from-Motion

Jiankun Zhong^{*1,3}, Zitong Zhan^{*2}, Quankai Gao^{*1}, Ziyu Chen¹, Haozhe Lou¹,
Jiageng Mao¹, Ulrich Neumann¹, and Yue Wang¹

¹University of Southern California

²University at Buffalo

³Tsinghua University

Abstract—Structure-from-Motion (SfM), a method that recovers camera poses and scene geometry from uncalibrated images, is a central component in robotic reconstruction and simulation. Despite the state-of-the-art performance of traditional SfM methods such as COLMAP and its follow-up work, GLOMAP, naïve CPU-specialized implementations of bundle adjustment (BA) or global positioning (GP) introduce significant computational overhead when handling large-scale scenarios, leading to a trade-off between accuracy and speed in SfM. Moreover, the blessing of efficient C++-based implementations in COLMAP and GLOMAP comes with the curse of limited flexibility, as they lack support for various external optimization options. On the other hand, while deep learning-based SfM pipelines like VGGsFm and VGGT enable feed-forward 3D reconstruction, they are unable to scale to thousands of input views at once as GPU memory consumption increases sharply as the number of input views grows. In this paper, we unleash the full potential of GPU parallel computation to accelerate each critical stage of the standard SfM pipeline. Building upon recent advances in sparse-aware bundle adjustment optimization, our design extends these techniques to accelerate both BA and GP within a unified global SfM framework. Through extensive experiments on datasets of varying scales (e.g. 5000 images where VGGsFm and VGGT run out of memory), our method demonstrates up to $\sim 40\times$ speedup over COLMAP while achieving consistently comparable or even improved reconstruction accuracy. Our project page can be found at <https://cre185.github.io/InstantSfM/>.

I. INTRODUCTION

Structure-from-Motion (SfM) has played a key role in robotics, enabling the reconstruction of 3D scenes from well-captured multi-view images or even unorganized Internet photographs [1], [2]. This technique paves the way for applications ranging from multi-view stereo (MVS) [3] with dense reconstruction, digital heritage [4] to even dynamic scene reconstruction [5]–[7]. It also promotes recent advances in implicit neural representations such as neural radiance field (NeRF) [8] and 3D Gaussian splatting (3DGS) [9]. They have demonstrated impressive capabilities in novel view synthesis and 3D reconstruction, but depend on the SfM to provide a camera calibration or the complete initial scene geometry. Using geometric consistency across overlapping views, SfM simultaneously estimates both camera parameters and the underlying scene structure. In particular, global SfM methods optimize all camera poses and scene points simultaneously, offering superior accuracy and consistency compared to incremental approaches that construct the model sequentially and

are susceptible to error accumulation, or drift, over time [10]. However, this comprehensive optimization comes at the cost of significantly higher computational demands, especially when processing large-scale datasets, necessitating advanced strategies to improve efficiency. Despite notable advancements in feature detection [11] and optimization algorithms [12]–[14], the challenge of computational scalability persists, driving ongoing research in the field. Fundamentally, camera pose estimation with hundreds or even thousands of images usually involves solving massive-scale non-linear least squares problems in BA and GP. They are computationally heavy as the iterative optimization requires calculating large-sized Jacobian *w.r.t.* all camera parameters and 3D triangulation points.

To address this critical issue, we present InstantSfM, a comprehensive exploration of developing up-to-date SfM methodologies using modern GPU techniques, enabling fully sparse and parallel optimization on a single GPU without the need for a distributed cluster [1]. Building upon prior work in GPU-based sparse bundle adjustment [15], our approach introduces an entire SfM optimization pipeline in PyTorch, offering full operator coverage for the SfM process. This implementation requires significant technical innovation as the sparse Jacobian becomes very large when the input images are numerous, requiring customized Lie group and Lie algebra implementations. For example, we implement differentiable quaternion addition and large matrix multiplication for efficient element fetching—features not natively supported in PyTorch. In addition, our system is user-friendly and enables seamless plug-and-play integration with other user-specific PyTorch/Python packages. We validate our approach through extensive experiments on diverse and real-world datasets. Our work directly addresses the computation bottleneck in global SfM and delivers state-of-the-art accuracy with dramatically improved efficiency, making it scalable to datasets comprising thousands of images. Our contributions are as follows:

- We extend sparse-aware bundle adjustment techniques to global positioning, introducing a complete global SfM system in PyTorch;
- We demonstrate state-of-the-art efficiency while achieving comparable accuracy to both traditional well-established SfM pipelines and learning-based methods;

*These authors contributed equally to this work.

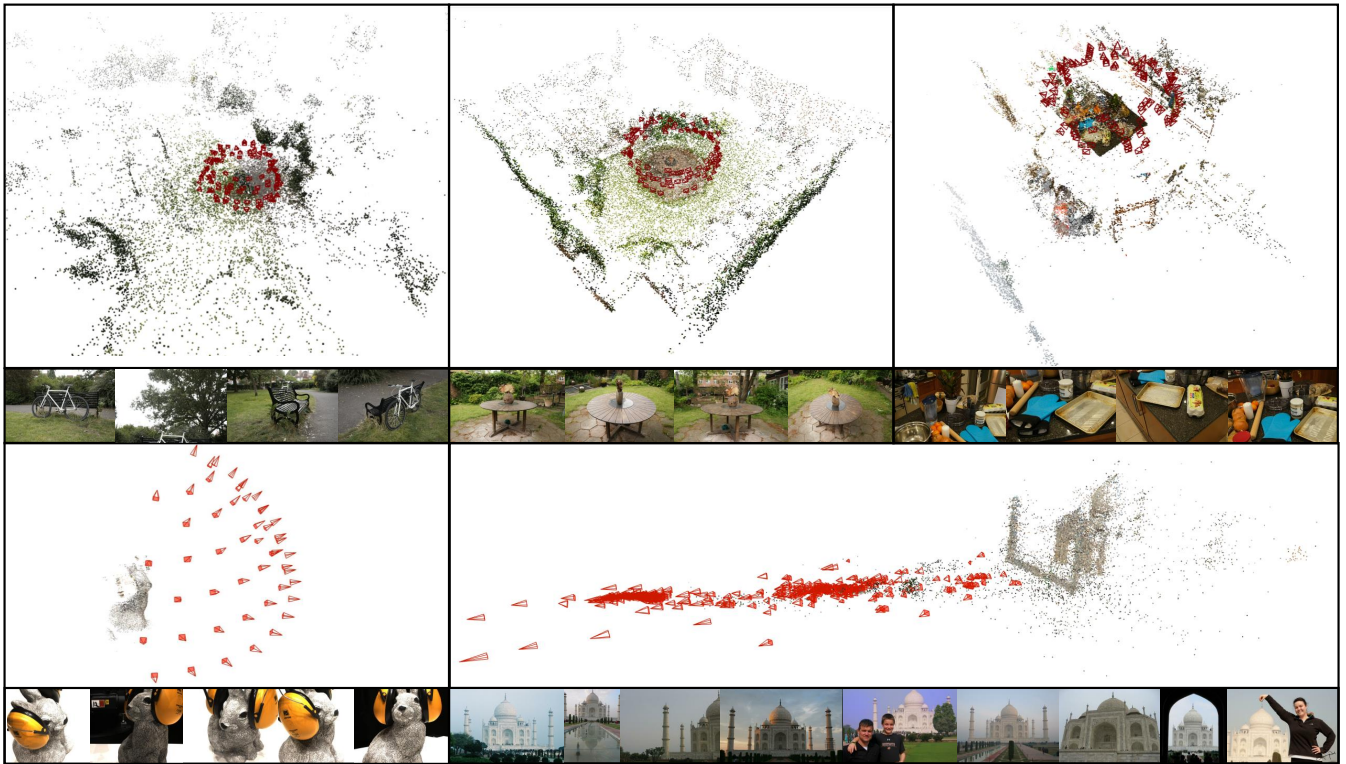


Fig. 1. Qualitative results on various datasets. Camera frustums as red are visualized for illustrating the estimated camera poses. Input images for each scene are sampled below each reconstruction.

- We incorporate depth prior into the optimization so that camera parameters and 3D point clouds are recovered at metric scale. InstantSfM significantly outperforms compared methods on several datasets.

II. RELATED WORK

A. Structure from Motion

Correspondence Search. SfM begins with feature detection on a given image set, denoted as $\mathcal{I} = \{I_1, \dots, I_n\}$, and extracts either sparse [16], [17] or dense [18], [19] feature descriptors $\mathcal{F} = \{f_1, \dots, f_n\}$ to establish view correspondences. The feature detections are then matched by calculating the feature affinities or more advanced matching algorithms [20]. Based on these matching results, homography \mathbf{H} and fundamental matrix \mathbf{F} are estimated to model pairwise view transformations. Since outliers are inevitably involved in feature extraction, robust estimation algorithms such as RANSAC [21] can greatly improve the accuracy of correspondence search.

Reconstruction. Given the estimated scene graph from the correspondence search, the reconstruction step aims to recover the intrinsic and extrinsic camera parameters, along with the scene structure represented as a set of 3D points triangulated from 2D features [22]. For estimating camera parameters, one prevalent option is incremental reconstruction [1], [23], [24], which progressively integrates pairwise view transformations into the existing 3D map reconstruction. Incremental approaches are well-known to be robust against outliers as it iteratively filters outlier and refines pose, but they also suffer from drift and low computational efficiency [25]. Global approaches [26]–[29] estimate all 3D points and camera poses

at once. They employ strategies such as rotation averaging and global positioning, which provide an initial guess of camera poses for BA. Although global SfM approaches may lack per-step outlier filtering or rejection, various designs have been proposed to mitigate drift and error. These methods incorporate 3D cues such as reference planes, line segments, and vanishing points or employ re-triangulation to enhance the robustness of BA.

Learning-Based SfM. Significant progress has been made in learning-based SfM, including end-to-end differentiable SfM pipelines such as VGGsFm [30]. An orthogonal line of research [31], [32] approaches the same goal in a feedforward manner by leveraging pretrained image-3D encoder such as DUS3R [33]. However, these methods are either computationally expensive in terms of time and memory, limited to small- and moderate-scale scenes, or lack guarantees for generalization to out-of-distribution cases.

B. Non-Linear Optimization

Bundle Adjustment (BA) is a key optimization method used to refine camera parameters and 3D scene structure by minimizing the reprojection error, which represents the 2D pixel difference between the observed points in the images and the projections of the estimated 3D points onto those images. The reprojection error for each 3D point is evaluated across all images where the point is visible. The classic BA formulation involves adjusting both the camera poses and the 3D point positions to minimize the total sum of these errors across all points and images, thereby improving the accuracy and consistency of the 3D

reconstruction [11]. It boils down to solving a non-linear least squares problems, whose size scales with the number of images and 3D points. Since there is no general closed-form solution, most of the literature focuses on developing efficient second-order numerical solvers for BA, ranging from Gauss-Newton methods to the more robust Levenberg-Marquardt (LM) algorithm [34]. Widely-used BA frameworks are either C++-based, enabling parallelization on CPU such as Ceres [35] and GTSAM [36], or PyTorch implementations such as DeepLM [37], which utilize PyTorch’s autograd engine for Jacobian calculations.

Recent work has explored GPU-based sparse bundle adjustment optimizations [15], demonstrating significant acceleration through sparse matrix operations and cuSPARSE implementations for BA problems. Building upon these sparse-aware techniques, we extend the approach to encompass both bundle adjustment and global positioning within a unified PyTorch framework. Although existing tools achieve high accuracy, they either remain inefficient for large-scale BA problems [38] or cannot generalize to more types of problems such as GP [37]. An orthogonal line of research, such as [39], proposes a convex relaxation of the original BA objective; however, it relies on monocular depth estimation and is not designed to handle outliers. Our work builds upon established sparse-aware BA techniques and extends them to accelerate both GP and BA in a comprehensive SfM pipeline.

III. GLOBAL SFM PIPELINE

While a general global SfM consists of multiple steps from feature matching to BA, we highlight our main contributions that focus on sparse-aware optimization for non-linear least squares in GP and BA. In this section, we firstly introduce the preliminaries including the general formulations of GP and BA, and then we investigate the inherently sparse Jacobian of the reprojection error. Finally, we detail our contribution about sparse-aware optimization for GP and BA.

A. Global Camera Pose Estimation

Global camera pose estimation plays an important role in initializing camera extrinsics before iterative BA. It consists of rotation averaging [40] and translation averaging [27], [41]. It is worth mentioning that GLOMAP proposes GP as a more robust alternative to translation averaging by jointly estimating locations of camera centers and 3D points with fixed camera rotations. Denote the number of cameras and points by C and P , respectively. The optimization objective can be formulated as follows:

$$\theta = \arg \min_{\mathbf{X}, \mathbf{t}, d} \sum_{i=1}^C \sum_{j=1}^P \rho(\| \underbrace{\mathbf{v}_{ij} - d_{ij}(\mathbf{X}_j - \mathbf{t}_i)}_{\mathbf{u}_{ij}} \|_2^2), \quad (1)$$

where optimizable parameters θ include 3D point locations $\mathbf{X} \in \mathbb{R}^{P \times 3}$, camera centers $\mathbf{t} \in \mathbb{R}^{C \times 3}$ and scalar scales d_{ij} for every valid observation; ρ is Huber [42] robustifier and \mathbf{v} denotes pixel ray direction vectors from camera centers to 2D feature points. After convergence, each triangulated 3D point \mathbf{X}_k should lie in its corresponding pixel ray emitted from visible cameras ensuring global consistency.

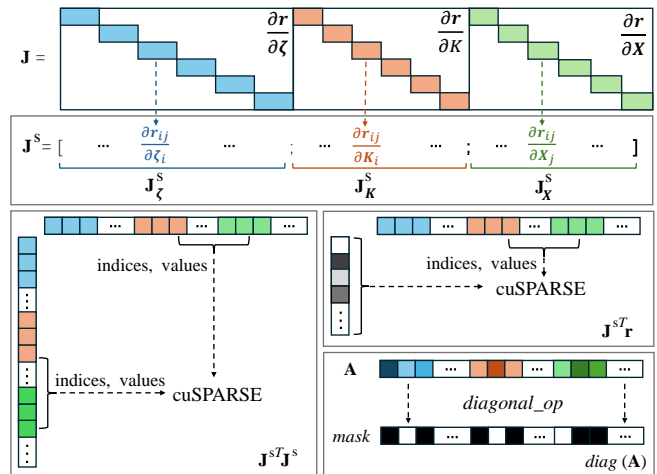


Fig. 2. We illustrate the sparse representation of Jacobian \mathbf{J}^S and sparse-aware operations for fast LM optimization, including sparse matrix-matrix multiplication $\mathbf{A} = \mathbf{J}^{S^T} \mathbf{J}^S$, sparse-dense matrix-vector multiplication $\mathbf{J}^{S^T} \mathbf{r}$, and diagonal operations such as element fetching $\text{diag}(\mathbf{A})$, where both are implemented with [15]. White elements are all with zero values.

B. Bundle Adjustment

Global camera pose estimation estimates camera rotations, camera centers, and 3D points independently with limited accuracy. BA can further refine the above estimations together with camera intrinsics. Similar to GP, BA is formulated as the least squares problem, minimizing the reprojection errors $\mathbf{r} \in \mathbb{R}^{2 \times CP}$ of 3D points across visible camera views:

$$\theta = \arg \min_{\mathbf{X}, \zeta, \mathbf{K}} \sum_{i=1}^C \sum_{j=1}^P \rho(\| \underbrace{\Pi(\zeta_i, \mathbf{X}_j, \mathbf{K}_i) - \mathbf{x}_{ij}}_{\mathbf{r}_{ij}} \|_2^2), \quad (2)$$

where optimizable parameters θ include camera intrinsics $\mathbf{K} \in \mathbb{R}^{C \times 1}$ and extrinsics $\zeta = \{\mathbf{t}, \mathbf{o}\} \in \mathbb{R}^{C \times 7}$ consisting of camera centers $\mathbf{t} \in \mathbb{R}^{C \times 3}$ and quaternions $\mathbf{o}_i \in \mathbb{S}\mathbb{O}(3)$. \mathbf{r}_{ij} denotes the reprojection error between a 2D feature point \mathbf{x}_{ij} on the i -th camera and the j -th 3D point \mathbf{X}_j projected to the same camera. We describe our approach of solving the two optimization problems in method.

IV. METHOD

A. Levenberg-Marquardt Algorithm

Levenberg-Marquardt (LM) algorithm is a widely used second-order method for solving non-linear least squares problems. We use LM for the optimization objectives of GP and BA. Specifically, the LM algorithm uses the Jacobian of the optimization goal and solves the following linear system for an update step $\Delta\theta$,

$$(\mathbf{J}^T \mathbf{J} + \lambda \text{diag}(\mathbf{J}^T \mathbf{J})) \Delta\theta = -\mathbf{J}^T \mathbf{r}, \quad (3)$$

where $\mathbf{J} = \frac{\partial \mathbf{r}}{\partial \theta}$ is the Jacobian matrix. We take BA for illustration to show the structure of the Jacobian. Each row of the matrix stores the gradient of a 2D reprojection *w.r.t.* all parameters. Collectively, the entire Jacobian matrix that exhaustively stores every gradient will have a shape of $\mathbf{J} \in \mathbb{R}^{2CP \times (7C+3P)}$. This matrix is large even under moderate-scale reconstruction, making it infeasible to store in GPU

Algorithm 1 The Levenberg-Marquardt algorithm

Require: λ (damping), θ_0 (params)

```
for  $t \leftarrow 1$  to  $T$  do
   $\mathbf{J} \leftarrow \frac{\partial \mathbf{r}_{\theta_{t-1}}}{\partial \theta_{t-1}}$ 
   $\mathbf{A} \leftarrow \mathbf{J}^\top \mathbf{J}$ 
   $\mathbf{A} \leftarrow \mathbf{A} + \lambda \cdot \text{diag}(\mathbf{A})$ 
   $\Delta \theta = \text{solver}(\mathbf{A}, -\mathbf{J}^\top \mathbf{r})$ 
   $\theta_t \leftarrow \theta_{t-1} + \Delta \theta$ 
end for
return  $\theta_t$ 
```

memory. The Schur complement trick [12] could reduce the amount of computation but does not improve the spatial complexity.

In addition, the LM algorithm requires iterative matrix operations to update optimizable parameters θ as shown in . The data scale of \mathbf{J} will affect the running time of the entire algorithm. However, the commonly used SfM pipeline [23] can only solve the optimization in dense matrix format on GPU. Building upon established sparse-aware BA techniques, we extend the sparse data structure approach to encompass global positioning in addition to bundle adjustment, creating a unified framework for both optimization stages.

B. Sparse Jacobian

The Jacobian matrix \mathbf{J} records the gradients for reprojection error *w.r.t.* optimizable parameters, e.g. camera intrinsics, extrinsics, 3D point locations, occupy exactly 3 blocks in each Jacobian row, with the rest of the values being empty. Additionally, each 3D point is observed by only a limited number of cameras. If a 3D point is occluded or falls out of the camera’s field of view, the corresponding Jacobian will be zero. This visibility consideration significantly reduces the number of rows in the Jacobian matrix. Therefore, the Jacobian matrix \mathbf{J} is highly sparse. For instance, consider a scene with approximately 200 images, the Jacobian matrix \mathbf{J} has a size on the order of 10^{10} , while only about 10^6 elements are non-zero. This results in a sparse block-diagonal structure [15], as shown in Fig. 2. This sparse nature, previously explored in GPU-based bundle adjustment, arises because each 2D observation is tied with exactly one camera, one 3D point, and one intrinsic parameter.

According to Algorithm 1, each LM loop involves 1) large-scale matrix-matrix multiplication $\mathbf{J}^\top \mathbf{J}$; 2) large-scale matrix-vector multiplication; 3) diagonal element fetching $\text{diag}(\mathbf{A})$; 4) a linear solver $\Delta \theta = \text{solver}(\mathbf{A}, -\mathbf{J}^\top \mathbf{r})$ to solve a linear system formulated as $\mathbf{A} \Delta \theta = -\mathbf{J}^\top \mathbf{r}$. Storing and computing with \mathbf{J} using a sparse data structure would reduce both spatial complexity and computational cost across all operations.

Despite the high spatial complexity of the Jacobian matrix \mathbf{J} , each non-zero block is small and independent, e.g. $\frac{\partial \mathbf{r}_{ij}}{\partial \zeta_i} \in \mathbb{R}^{2 \times 7}$ and $\frac{\partial \mathbf{r}_{ij}}{\partial \mathbf{X}_j} \in \mathbb{R}^{2 \times 3}$. This inspires us to distribute non-zero Jacobian blocks across different GPU computing units, enabling full parallel calculations and making tensor indexing

efficient in LM loops. To this end, we first store the Jacobian matrix in its sparse form \mathbf{J}^s by retaining only its non-zero values along with their corresponding indices. This reduces the spatial complexity from $\mathcal{O}(n^2)$ to $\mathcal{O}(n)$, where $n \approx P$ under the common assumption that $P \gg C$ (i.e., the number of 3D points far exceeds the number of cameras). Consequently, we propose several sparsity-aware operations to accelerate the LM algorithm, summarized in Sec. IV-D.

C. Optimization with Depth Prior

Our pipeline allows for injecting depth information into the optimization as estimating camera poses and 3D representations at metric scale is particularly important when reconstructed objects and environments must be interactable with robots in a simulator. For example, a robot’s gripper should be larger than an apple either in the real world or in a virtual simulator. As in Eq. 1, the 2D projection \mathbf{v}_{ij} of a 3D point \mathbf{X}_j observed at i -th image is inherently normalized during the optimization so that $\|\mathbf{v}_{ij}\| = 1$. However, the true value of this scale ratio should be depth-dependent. Therefore, we replace the optimizable scale term d_{ij} in Eq. 1 with $d_{ij} = 1/\text{depth}_{ij}$, where depth_{ij} is sampled from the estimated or ground-truth depth map of i -th camera viewpoint.

Then the reprojection error with depth prior can then be expressed as:

$$\mathbf{u}_{ij} = \mathbf{v}_{ij} - \frac{\mathbf{X}_j - \mathbf{t}_i}{\text{depth}_{ij}} \quad (4)$$

D. Implementation

Building upon established sparse-aware bundle adjustment frameworks [15], we detail the specific implementation choices and optimizations for our complete SfM pipeline.

Depth-Constrained Jacobian Structure. When incorporating monocular depth priors, we extend the standard (2×7) and (2×3) Jacobian blocks to include depth constraint terms. This requires specialized block assembly routines that handle the additional geometric constraints while preserving sparse matrix efficiency.

Cross-Stage Memory Management. Unlike traditional BA-only implementations, our complete SfM pipeline requires maintaining sparse representations across global positioning and bundle adjustment stages. We implement a unified memory pool system that reuses sparse matrix storage and avoids costly memory reallocations between optimization phases.

Robust Outlier Integration. Our sparse implementation incorporates robust loss functions directly into the sparse matrix operations through element-wise masking inside the second-order optimization. Therefore, if a parameter does not introduce meaningful gradient in the forward pass, the optimization stage will automatically remove the parameter so that it does not introduce singularity to the linear system. This eliminates the need for dense intermediate computations typically required for outlier handling in traditional implementations.

TABLE I

COMPARISON ON THE MIPNeRF360 DATASET [43] USING THE NVS METRIC. ALL EXPERIMENTS USE *images_4* FROM THE DATASET, WHICH IS 4× DOWNSAMPLED FROM THE ORIGINAL 4K RAW DATA, RESULTING IN AROUND 1K RESOLUTION.

	PSNR ↑				SSIM ↑				LPIPS ↓			
	COLMAP	GLOMAP	VGGsFM	Ours	COLMAP	GLOMAP	VGGsFM	Ours	COLMAP	GLOMAP	VGGsFM	Ours
bicycle	20.75	25.97	25.81	25.73	0.576	0.791	0.783	0.780	0.384	0.156	0.162	0.162
bonsai	19.86	32.96	32.56	32.06	0.619	0.957	0.953	0.947	0.490	0.054	0.056	0.061
counter	29.10	29.26	29.29	29.23	0.913	0.916	0.916	0.915	0.092	0.091	0.092	0.092
garden	27.91	27.80	27.74	27.66	0.878	0.876	0.875	0.869	0.072	0.073	0.073	0.077
kitchen	32.09	16.11	15.96	27.79	0.947	0.388	0.390	0.845	0.046	0.880	0.878	0.117
room	31.54	31.96	31.91	31.04	0.936	0.937	0.936	0.925	0.085	0.083	0.085	0.102
stump	27.21	26.61	26.51	25.53	0.797	0.760	0.758	0.711	0.143	0.164	0.168	0.184
Average	26.92	● 27.24	27.11	● 28.43	0.809	● 0.804	0.802	● 0.856	● 0.187	0.214	0.216	● 0.113

TABLE II

QUANTITATIVE EVALUATION FOR SfM METHODS ON DTU DATASET.

	PSNR ↑			SSIM ↑			LPIPS ↓		
	COLMAP	GLOMAP	Ours	COLMAP	GLOMAP	Ours	COLMAP	GLOMAP	Ours
scan002	21.83	20.77	22.80	0.872	0.862	0.868	0.094	0.166	0.096
scan016	24.94	24.18	24.04	0.892	0.891	0.899	0.075	0.237	0.067
scan033	23.45	7.192	22.11	0.911	0.356	0.907	0.075	0.860	0.081
scan047	22.91	7.470	24.49	0.909	0.409	0.913	0.104	0.510	0.091
scan062	23.71	25.85	25.56	0.907	0.919	0.909	0.076	0.248	0.070
scan077	23.40	13.41	21.50	0.928	0.715	0.907	0.100	0.882	0.140
scan095	24.00	17.49	20.80	0.867	0.659	0.769	0.153	0.693	0.240
scan109	30.13	28.32	28.98	0.911	0.902	0.901	0.151	0.166	0.158
scan123	30.64	17.16	30.83	0.910	0.580	0.913	0.212	0.228	0.211
Average	● 25.00	17.98	● 24.57	● 0.901	0.699	● 0.887	● 0.116	0.443	● 0.128

V. EXPERIMENT

Since the deep learning-based baseline VGGsFM [30] encounters out-of-memory issues on an NVIDIA RTX 4090 (24GB) when processing more than 50 images, we conduct comparisons of VGGsFM, COLMAP, GLOMAP, and our InstantSfM on a platform equipped with an Intel Xeon Platinum 8480C and an NVIDIA H200 GPU (140.4 GB). For a fair comparison with COLMAP and GLOMAP, we use RootSIFT for feature extraction. It is worth noting that our pipeline supports a variety of learning-based feature descriptors, such as [18], [11], and [17], directly in Python, without requiring conversion to C++. Qualitative results on various datasets are shown in Fig. 1.

Evaluation Criteria. We focus on three types of evaluation metrics: (a) camera pose estimation, (b) rendering quality with 3DGS [44], and (c) 3D map reconstruction accuracy. For datasets with ground-truth camera pose, we report the Area Under the Recall Curve (AUC) scores, following previous works [26], [45]. For unordered image data, such as Tanks and Temples dataset, AUC is calculated as the pairwise relative rotation error between the given ground-truth poses and ours. For datasets that do not provide such ground-truth, we report novel view synthesis (NVS) metrics (e.g., PSNR, SSIM, and LPIPS) by training 3D Gaussian Splatting [9] (3DGS) using the estimated camera poses and 3D map reconstruction points as an initialization. Lastly, we also measure the Chamfer distance on datasets with reliable ground-truth point cloud scan to demonstrate 3D map reconstruction accuracy.

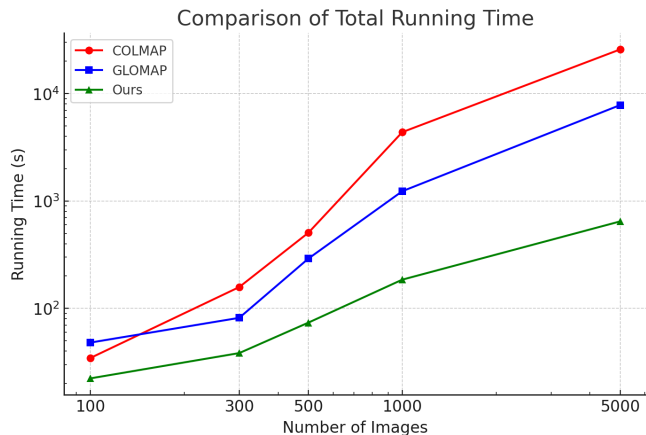


Fig. 3. Comparisons of total SfM running time among COLMAP, GLOMAP and InstantSfM on different numbers of images. Running time is in log space.

A. Datasets and Results

MipNeRF360 [43] consists of 7 different scenes where cameras capture a central object from a full 360-degree perspective. The number of images of each scene ranges from 125 to 311. The dataset contains calibrated camera poses and SfM points from COLMAP. We train 3DGS on SfM results and report NVS metrics in and qualitative results in . Since VGGsFM uses 1K resolution by default, we conduct all experiments using “images_4” for fair comparisons. These images are downsampled by a factor of 4 from the original 4K or 6K resolution. We report NVS rendering metric in Tab.I.

DTU [47], [48] This object-centric dataset consists of 119

TABLE III
QUANTITATIVE EVALUATION FOR SfM METHODS ON TANKS AND TEMPLES INTERMEDIATE DATASETS.

	AUC @ 3 ↑			AUC @ 5 ↑			AUC @ 10 ↑			AUC @ 20 ↑		
	COLMAP	GLOMAP	Ours	COLMAP	GLOMAP	Ours	COLMAP	GLOMAP	Ours	COLMAP	GLOMAP	Ours
Family	72.91	73.37	70.11	84.86	85.01	83.11	87.28	87.37	85.76	89.09	89.14	87.77
Francis	62.10	62.01	62.50	81.01	81.02	80.48	84.93	84.94	84.32	87.91	87.91	87.30
Horse	68.04	68.51	62.48	83.21	83.39	80.17	86.29	86.40	83.93	88.60	88.65	86.79
Lighthouse	58.07	58.65	53.99	78.67	78.86	76.58	83.35	83.48	81.84	87.04	87.12	86.04
M60	57.59	59.48	57.40	79.16	79.97	78.91	83.77	84.27	83.42	87.30	87.56	86.85
Panther	35.33	35.19	37.25	71.60	71.72	72.37	79.25	79.33	79.71	85.06	85.10	85.29
Playground	26.76	26.53	14.00	69.31	68.87	58.11	77.94	77.44	69.99	84.42	83.87	79.62
Train	59.21	59.33	52.50	80.00	80.06	75.33	84.30	84.34	80.58	87.57	87.59	84.90
Average	55.00	55.38	51.28	78.48	78.61	75.63	83.39	83.45	81.19	87.12	87.12	85.57

TABLE IV

CHAMFER DISTANCE COMPARISON ON SCANNET. LOWER IS BETTER.

FAILED INDICATES AN OPTIMIZATION FAILURE, RESULTING IN NO CAMERA POSES OR POINT CLOUD OUTPUT. DUE TO TIME CONSTRAINTS, COLMAP WAS NOT TESTED ON SCAN 0002_01. OURS (W/O DEPTH) DENOTES INSTANTSfM RESULT WITHOUT USING DEPTH PRIOR WHILE OURS (W/ DEPTH) DENOTES INSTANTSfM USING DEPTH PRIOR IN OPTIMIZATION.

	COLMAP	GLOMAP	Ours (w/o depth)	Ours (w/ depth)
0001_00	3.358	FAILED	0.557	0.987
0001_01	FAILED	FAILED	0.768	0.646
0002_00	FAILED	FAILED	0.244	0.208
0002_01	FAILED	FAILED	0.205	0.195
0003_00	0.4139	FAILED	2.353	1.098
0003_01	0.2478	FAILED	1.211	1.047
0003_02	0.2337	FAILED	0.556	0.428
Average	FAILED	FAILED	0.842	0.658

TABLE V

CHAMFER DISTANCE COMPARISON ON RANDOMLY PICKED SCANS FROM SCANNET++. * CORRESPONDS TO COLMAP (ORACLE GEOMETRY), WHICH DENOTES THE 3D RECONSTRUCTION OBTAINED FROM RENDERED VIRTUAL IMAGES WITH CAMERA POSE REFINEMENT GUIDED BY THE LASER SCAN GEOMETRY IN [46].

	*COLMAP	COLMAP	GLOMAP	Ours
0f69ae...	*0.14	FAILED	1.67	0.92
ff1765...	*0.21	2.38	3.85	2.71
8c3169...	*0.16	FAILED	3.36	1.05
00777c...	*0.33	FAILED	5.38	5.22
00a231...	*0.25	FAILED	4.74	3.15
Average	*0.22	FAILED	3.80	2.61

scans, each with different lighting conditions. We select the medium lighting condition (condition 5) as our evaluation benchmark. In addition, the dataset provides ground-truth geometry obtained through structured light scanning. We train 3DGS on SfM results and report the NVS metric in Tab. II

Tanks and Temples [49] consists of 8 scenes from the Intermediate dataset. Evaluation is performed on uniformly sampled frames from captured videos, *i.e.* 150 frames for Family and Horse and 300 for all other scenes. We report quantitative results in Tab. III. Our method does not outperform COLMAP or GLOMAP, and we observed

that several estimated camera poses in the underperforming scenes suffer from an intrinsics–translation ambiguity. In these cases, the estimated cameras have larger intrinsics and are positioned farther from their correct locations. For example, in the Playground scene, a few of our cameras show noticeable misalignment, with their intrinsic parameters deviating by up to approximately 25% from those of normally positioned cameras. There are two possible reasons: (1) our ViewGraphCalibration step is implemented with PyCeres, which differs slightly from the C++ Ceres implementation used in COLMAP and GLOMAP; (2) COLMAP estimates relative camera poses after the ViewGraphCalibration step using PoseLib in C++, whereas our implementation relies on OpenCV in Python, leading to differences in implementation details.

ScanNet [50] and **ScanNet++** [46] provide comprehensive collections of RGB-D scans capturing a diverse range of real-world indoor environments. We randomly pick 7 and 5 out of 1000+ scans from ScanNet and ScanNet++ and report quantitative results in Tab. IV and Tab. V, respectively. For experiments on ScanNet, both COLMAP and GLOMAP exhibit varying degrees of failure in the tested scenes, while our InstantSfM shows significantly better robustness in terms of optimization and performs better with depth prior. The failure of GLOMAP stems from solver failures in its ViewGraphCalibration step, where the underlying Ceres solver encounters consecutive optimization iterations that fail to meet convergence criteria. When the number of consecutive failed optimization attempts exceeds a predefined threshold, the Ceres framework terminates the entire pipeline to prevent numerical instability. This termination mechanism prevents the subsequent SfM pipeline from proceeding normally, resulting in complete reconstruction failure. COLMAP’s failure, on the other hand, results from poor reconstruction quality (successful reconstruction on only a few cameras), preventing it from aligning to the ground truth data and making it impossible to compute metrics correctly. For experiments on ScanNet++, our InstantSfM consistently outperforms GLOMAP. When running COLMAP’s without oracle geometry, it fails on all scenes except ff17657f71.

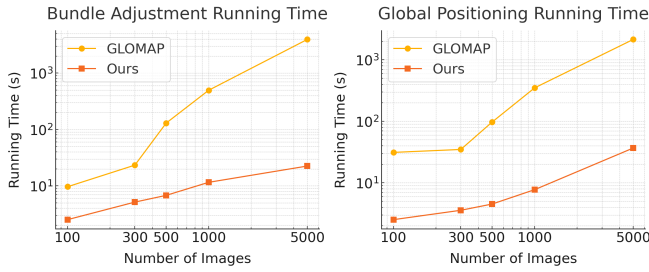


Fig. 4. Comparisons of BA and GP running time between GLOMAP and InstantSfM on different numbers of images to be calibrated. Running time is in log space.

B. Running Time Analysis

Runtime Comparisons with COLMAP and GLOMAP.

To demonstrate the high efficiency of our method on SfM tasks, we compare its running time with COLMAP and GLOMAP on scenes ranging from 100 to 5,000 images, as shown in Fig. 4. Specifically, scenes with 100 images are selected from the MipNeRF360 [43] dataset through downsampling, while larger scenes (300-5,000 images) are obtained by downsampling from the 1DSfM [13] dataset. This selection strategy is adopted because the 1DSfM dataset, with its large-scale scenes, would be difficult to effectively match when downsampled to only 100 images.

Runtime Comparisons with Other GPU-based Methods.

We report runtime comparisons of GPU-based BA in Tab. VI on the standard **BA** in the **Large** dataset (BAL), where PBA results are from the DeepLM paper and Weber et al. reported their own performance on a subset of BAL. All other baselines are tested on the same hardware.

TABLE VI
RUNTIME(S) COMPARISON WITH GPU BASED METHODS.

Dataset	Ceres-GPU	PBA	DeepLM	Weber	Ours
Trafalgar	8.5	16.8	2.3	No Report	0.8
Ladybug	56.9	12.3	2.7	No Report	2.1
Dubrovnik	19.0	25.5	2.6	≥ 17	1.7

Next, we report comparison with GPU-based SfM libraries, including GLOMAP and COLMAP. Notably, GLOMAP only added GPU support since March 20, 2025. Tests were conducted on 3 randomly selected scenes from 1DSfM dataset due to significant time for feature processing. Despite demonstrable efficiency improvements with added GPU acceleration, COLMAP and GLOMAP still lag behind our method, as shown in Tab. VII.

TABLE VII
GPU RUNTIME(S) COMPARISON WITH COLMAP/GLOMAP

Dataset	COLMAP	GLOMAP	Ours
Alamo	12855.4	1599.5	597.0
Madrid_Metropolis	1661.5	440.7	222.9
Union_Square	4696.7	966.4	571.3

VI. CONCLUSION

In this paper, we presented InstantSfM, a fast yet easy-to-use Structure-from-Motion pipeline that leverages sparsity-aware operations natively in PyTorch. Our approach achieves significant speedups compared to existing methods while maintaining or improving reconstruction quality and robustness. Across various benchmark datasets, InstantSfM matches or surpasses the precision of both incremental and conventional global approaches while delivering substantially higher efficiency, especially for large-scale reconstructions. Our code will be made available as an open-source program under a community friendly license.

While the current implementation demonstrates promising results, it does have some limitations worth noting. First, 3D points' triangulation is not yet implemented with CUDA/Triton operators for acceleration, which could provide additional performance benefits. Secondly, the current pipeline is primarily designed for single-node execution but not distributed settings, which may limit its application to extremely large-scale problems. In future work, we plan to address these limitations and further explore the integration of learning-based features to improve reconstruction quality and efficiency.

REFERENCES

- [1] S. Agarwal, Y. Furukawa, N. Snavely, I. Simon, B. Curless, S. M. Seitz, and R. Szeliski, "Building rome in a day," *Communications of the ACM*, vol. 54, no. 10, pp. 105–112, 2011.
- [2] J.-M. Frahm, P. Fite-Georgel, D. Gallup, T. Johnson, R. Raguram, C. Wu, Y.-H. Jen, E. Dunn, B. Clipp, S. Lazebnik *et al.*, "Building rome on a cloudless day," in *Computer Vision—ECCV 2010: 11th European Conference on Computer Vision, Heraklion, Crete, Greece, September 5–11, 2010, Proceedings, Part IV 11*. Springer, 2010, pp. 368–381.
- [3] R. I. Hartley, R. Gupta, and T. Chang, "Stereo from uncalibrated cameras," in *CVPR*, vol. 92, 1992, pp. 761–764.
- [4] L. MacDonald, *Digital heritage*. Routledge, 2006.
- [5] Z. Chen, J. Yang, J. Huang, R. de Lutio, J. M. Esturo, B. Ivanovic, O. Litany, Z. Gojcic, S. Fidler, M. Pavone, L. Song, and Y. Wang, "Omni-nire: Omni urban scene reconstruction," in *The Thirteenth International Conference on Learning Representations*, 2025.
- [6] Z. Li, R. Tucker, F. Cole, Q. Wang, L. Jin, V. Ye, A. Kanazawa, A. Holynski, and N. Snavely, "Megasam: Accurate, fast, and robust structure and motion from casual dynamic videos," *arXiv preprint arXiv:2412.04463*, 2024.
- [7] H. Lou, Y. Liu, Y. Pan, Y. Geng, J. Chen, W. Ma, C. Li, L. Wang, H. Feng, L. Shi, L. Luo, and Y. Shi, "Robo-GS: A physics consistent spatial-temporal model for robotic arm with hybrid representation," in *IEEE International Conference on Robotics and Automation (ICRA)*, 2025. [Online]. Available: <https://arxiv.org/abs/2408.14873>
- [8] B. Mildenhall, P. P. Srinivasan, M. Tancik, J. T. Barron, R. Ramamoorthi, and R. Ng, "Nerf: Representing scenes as neural radiance fields for view synthesis," *Communications of the ACM*, vol. 65, no. 1, pp. 99–106, 2021.
- [9] B. Kerbl, G. Kopanas, T. Leimkühler, and G. Drettakis, "3d gaussian splatting for real-time radiance field rendering," *ACM Trans. Graph.*, vol. 42, no. 4, pp. 139–1, 2023.
- [10] R. A. Newcombe, S. Izadi, O. Hilliges, D. Molyneaux, D. Kim, A. J. Davison, P. Kohi, J. Shotton, S. Hodges, and A. Fitzgibbon, "Kinectfusion: Real-time dense surface mapping and tracking," in *2011 10th IEEE international symposium on mixed and augmented reality*. Ieee, 2011, pp. 127–136.
- [11] Z. Zhan, D. Gao, Y.-J. Lin, Y. Xia, and C. Wang, "iMatching: Imperative correspondence learning," in *European Conference on Computer Vision (ECCV)*, 2024. [Online]. Available: <https://arxiv.org/pdf/2312.02141.pdf>

- [12] S. Agarwal, N. Snavely, S. M. Seitz, and R. Szeliski, "Bundle adjustment in the large," in *Computer Vision—ECCV 2010: 11th European Conference on Computer Vision, Heraklion, Crete, Greece, September 5–11, 2010, Proceedings, Part II 11*. Springer, 2010, pp. 29–42.
- [13] K. Wilson and N. Snavely, "Robust global translations with ldsfm," in *European conference on computer vision*. Springer, 2014, pp. 61–75.
- [14] C. Zach, "Robust bundle adjustment revisited," in *Computer Vision – ECCV 2014*, D. Fleet, T. Pajdla, B. Schiele, and T. Tuytelaars, Eds. Cham: Springer International Publishing, 2014, pp. 772–787.
- [15] Z. Zhan, H. Xu, Z. Fang, X. Wei, Y. Hu, and C. Wang, "Bundle adjustment in the eager mode," *arXiv preprint arXiv:2409.12190*, 2024.
- [16] D. G. Lowe, "Distinctive image features from scale-invariant keypoints," *International journal of computer vision*, vol. 60, pp. 91–110, 2004.
- [17] J. DeTone, T. Malisiewicz, and A. Rabinovich, "Superpoint: Self-supervised interest point detection and description," in *Proceedings of the IEEE conference on computer vision and pattern recognition workshops*, 2018, pp. 224–236.
- [18] J. Sun, Z. Shen, Y. Wang, H. Bao, and X. Zhou, "Loft: Detector-free local feature matching with transformers," in *Proceedings of the IEEE/CVF conference on computer vision and pattern recognition*, 2021, pp. 8922–8931.
- [19] Y. Wang, X. He, S. Peng, D. Tan, and X. Zhou, "Efficient loft: Semidense local feature matching with sparse-like speed," in *Proceedings of the IEEE/CVF Conference on Computer Vision and Pattern Recognition*, 2024, pp. 21 666–21 675.
- [20] P.-E. Sarlin, D. DeTone, T. Malisiewicz, and A. Rabinovich, "Superglue: Learning feature matching with graph neural networks," in *Proceedings of the IEEE/CVF conference on computer vision and pattern recognition*, 2020, pp. 4938–4947.
- [21] M. A. Fischler and R. C. Bolles, "Random sample consensus: a paradigm for model fitting with applications to image analysis and automated cartography," *Communications of the ACM*, vol. 24, no. 6, pp. 381–395, 1981.
- [22] R. I. Hartley and P. Sturm, "Triangulation," *Computer vision and image understanding*, vol. 68, no. 2, pp. 146–157, 1997.
- [23] J. L. Schönberger and J.-M. Frahm, "Structure-from-motion revisited," in *Conference on Computer Vision and Pattern Recognition (CVPR)*, 2016.
- [24] N. Snavely, "Bundler: Structure from motion (sfm) for unordered image collections," Code available at <http://phototour.cs.washington.edu/bundler/>, 2010.
- [25] P.-E. Sarlin, M. Dusmanu, J. L. Schönberger, P. Speciale, L. Gruber, V. Larsson, O. Miksik, and M. Pollefeys, "LaMAR: Benchmarking Localization and Mapping for Augmented Reality," in *ECCV*, 2022.
- [26] L. Pan, D. Baráth, M. Pollefeys, and J. L. Schönberger, "Global structure-from-motion revisited," in *European Conference on Computer Vision*. Springer, 2024, pp. 58–77.
- [27] N. Jiang, Z. Cui, and P. Tan, "A global linear method for camera pose registration," in *Proceedings of the IEEE international conference on computer vision*, 2013, pp. 481–488.
- [28] P. Moulon, P. Monasse, and R. Marlet, "Global fusion of relative motions for robust, accurate and scalable structure from motion," in *Proceedings of the IEEE international conference on computer vision*, 2013, pp. 3248–3255.
- [29] Rother, "Linear multiview reconstruction of points, lines, planes and cameras using a reference plane," in *Proceedings Ninth IEEE International Conference on Computer Vision*. IEEE, 2003, pp. 1210–1217.
- [30] J. Wang, N. Karaev, C. Rupprecht, and D. Novotny, "Vggsfm: Visual geometry grounded deep structure from motion," in *Proceedings of the IEEE/CVF conference on computer vision and pattern recognition*, 2024, pp. 21 686–21 697.
- [31] Q. Wang, Y. Zhang, A. Holynski, A. A. Efros, and A. Kanazawa, "Continuous 3d perception model with persistent state," *arXiv preprint arXiv:2501.12387*, 2025.
- [32] J. Wang, M. Chen, N. Karaev, A. Vedaldi, C. Rupprecht, and D. Novotny, "Vggt: Visual geometry grounded transformer," in *Proceedings of the Computer Vision and Pattern Recognition Conference*, 2025, pp. 5294–5306.
- [33] S. Wang, V. Leroy, Y. Cabon, B. Chidlovskii, and J. Revaud, "Dust3r: Geometric 3d vision made easy," in *Proceedings of the IEEE/CVF Conference on Computer Vision and Pattern Recognition*, 2024, pp. 20 697–20 709.
- [34] A. Ranganathan, "The levenberg-marquardt algorithm," *Tutorial on LM algorithm*, vol. 11, no. 1, pp. 101–110, 2004.
- [35] S. Agarwal, K. Mierle *et al.*, "Ceres solver: Tutorial & reference," *Google Inc*, vol. 2, no. 72, p. 8, 2012.
- [36] F. Dellaert and G. Contributors, "borglab/gtsam," 2022.
- [37] J. Huang, S. Huang, and M. Sun, "DeepIm: Large-scale nonlinear least squares on deep learning frameworks using stochastic domain decomposition," in *Proceedings of the IEEE/CVF Conference on Computer Vision and Pattern Recognition*, 2021, pp. 10 308–10 317.
- [38] S. Agarwal, K. Mierle, and The Ceres Solver Team, "Ceres Solver," Oct. 2023. [Online]. Available: <https://github.com/ceres-solver/ceres-solver>
- [39] H. Han and H. Yang, "Building rome with convex optimization," *arXiv preprint arXiv:2502.04640*, 2025.
- [40] R. Hartley, J. Trunpf, Y. Dai, and H. Li, "Rotation averaging," *International journal of computer vision*, vol. 103, pp. 267–305, 2013.
- [41] V. M. Govindu, "Combining two-view constraints for motion estimation," in *Proceedings of the 2001 IEEE computer society conference on computer vision and pattern recognition. CVPR 2001*, vol. 2. IEEE, 2001, pp. II–II.
- [42] P. J. Huber, "Robust estimation of a location parameter," in *Breakthroughs in statistics: Methodology and distribution*. Springer, 1992, pp. 492–518.
- [43] J. T. Barron, B. Mildenhall, D. Verbin, P. P. Srinivasan, and P. Hedman, "Mip-nerf 360: Unbounded anti-aliased neural radiance fields," in *Proceedings of the IEEE/CVF conference on computer vision and pattern recognition*, 2022, pp. 5470–5479.
- [44] V. Ye, R. Li, J. Kerr, M. Turkulainen, B. Yi, Z. Pan, O. Seiskari, J. Ye, J. Hu, M. Tancik, and A. Kanazawa, "gsplat: An open-source library for Gaussian splatting," *arXiv preprint arXiv:2409.06765*, 2024. [Online]. Available: <https://arxiv.org/abs/2409.06765>
- [45] X. He, J. Sun, Y. Wang, S. Peng, Q. Huang, H. Bao, and X. Zhou, "Detector-free structure from motion," in *Proceedings of the IEEE/CVF Conference on Computer Vision and Pattern Recognition*, 2024, pp. 21 594–21 603.
- [46] C. Yeshwanth, Y.-C. Liu, M. Nießner, and A. Dai, "Scannet++: A high-fidelity dataset of 3d indoor scenes," in *Proceedings of the International Conference on Computer Vision (ICCV)*, 2023.
- [47] R. Jensen, A. Dahl, G. Vogiatzis, E. Tola, and H. Aanaes, "Large scale multi-view stereopsis evaluation," in *Proceedings of the IEEE Conference on Computer Vision and Pattern Recognition (CVPR)*, 2014.
- [48] H. Aanaes, R. R. Jensen, G. Vogiatzis, E. Tola, and A. B. Dahl, "Large-scale data for multiple-view stereopsis," *International Journal of Computer Vision*, pp. 1–16, 2016.
- [49] A. Knapitsch, J. Park, Q.-Y. Zhou, and V. Koltun, "Tanks and temples: Benchmarking large-scale scene reconstruction," *ACM Transactions on Graphics*, vol. 36, no. 4, 2017.
- [50] A. Dai, A. X. Chang, M. Savva, M. Halber, T. Funkhouser, and M. Nießner, "Scannet: Richly-annotated 3d reconstructions of indoor scenes," in *Proc. Computer Vision and Pattern Recognition (CVPR)*, IEEE, 2017.